Making Graphene *Holey*. Gold-Nanoparticle-Mediated Hydroxyl Radical Attack on Reduced Graphene Oxide

James G. Radich[†,‡] and Prashant V. Kamat[†,‡,§,*]

[†]Radiation Laboratory, [‡]Department of Chemical & Biomolecular Engineering, and [§]Department of Chemistry & Biochemistry, University of Notre Dame, Notre Dame, Indiana 46556, United States

ABSTRACT Graphene oxide (GO) and reduced graphene oxide (RGO) have important applications in the development of new electrode and photocatalyst architectures. Gold nanoparticles (AuNPs) have now been employed as catalyst to generate $OH^{\bullet}$ and oxidize RGO *via* hydroxyl radical attack. The oxidation of RGO is marked by pores and wrinkles within the 2-D network. Nanosecond laser flash photolysis was used in conjunction with competition kinetics to elucidate the oxidative mechanism and calculate rate constants for the AuNP-catalyzed and direct reaction between RGO and $OH^{\bullet}$. The results highlight the use of the AuNP-mediated oxidation reaction to tune the properties of RGO through the degree of oxidation and/or functional group selectivity in addition to the nanoporous and wrinkle facets. The ability of AuNPs to catalyze the photolytic decomposition of H_2O_2 as well as the hydroxyl radical-induced oxidation of RGO raises new issues concerning graphene stability in energy conversion and storage (photocatalysis, fuel cells, Li-ion batteries, *etc.*). Understanding RGO oxidation by free radicals will aid in maintaining the long-term stability of RGO-based functional composites where intimate contact with radical species is inevitable.

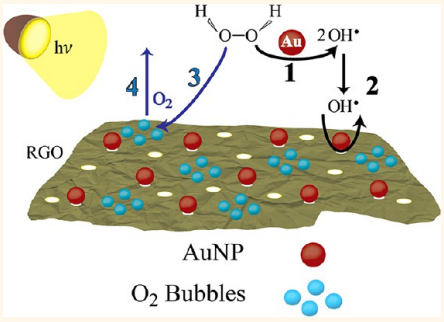

KEYWORDS: graphene · graphene oxide · reduced graphene oxide · hydroxyl radical · gold nanoparticles

In recent years, graphene has debuted as a highly studied carbon allotrope, owing to its large theoretical surface area of 2630 m^2/g, high intrinsic mobility of 200 000 $cm^2\ V^{-1}\ s^{-1}$,[1,2] and the exploration of various methods for preparing single- or few-layer sheets.[3−6] The unique electronic properties arise as a result of the 2-D hexagonal nature of the conjugated sp^2 network of carbon−carbon bonding, which gives rise to a conducting π band of $2p_z$ electrons that are oriented perpendicular to the bonding plane. Single-sheet graphene presents limitations in the ability to process bulk quantities, which limits this form of graphene to relatively specific applications at the present. Solution-based methods for single graphene sheets through dispersion of graphite layers have been reported,[7−10] but the oxidation of graphite to graphene oxide (GO) through some variant of Hummer's method[11] lends itself more favorably to functional graphene composites because of the ability to disperse single GO sheets in water and other solvents.[12,13]

The reduction of the electrically insulating GO to reduced graphene oxide (RGO) can be accomplished *via* thermal,[14,15] chemical,[16−18] electrochemical,[19−23] and photochemical processes.[24−29] Reduction of GO to RGO leads to a partially restored sp^2 network and therefore the partial restoration of electrical conductivity, the degree of which is dependent on the reduction method.[30] With the array of methods toward obtaining conductive RGO from GO and the ability to generate graphene-based functional composites from solution-based synthesis methods, this material is continually improving the performance of many energy conversion[25,31−38] and storage systems[39−51] involving complex photocatalyst or electrode designs. The inherent wrinkles in RGO sheets along with those produced during drying of

* Address correspondence to pkamat@nd.edu.

Received for review April 11, 2013 and accepted May 4, 2013.

Published online May 05, 2013
10.1021/nn401794k

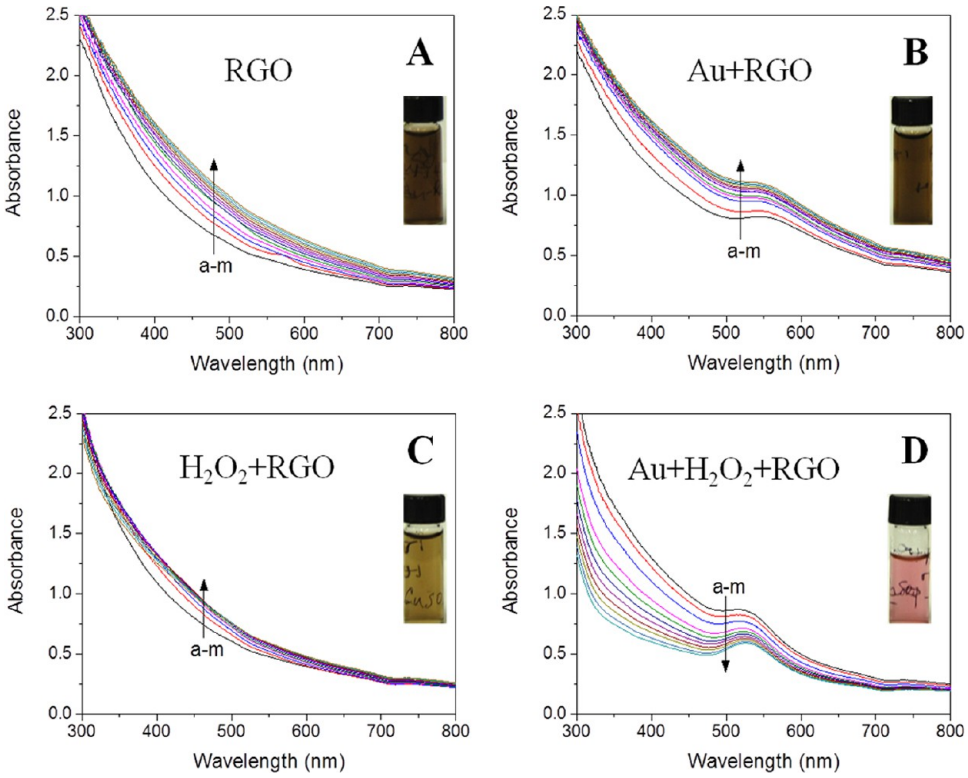

Figure 1. UV−visible absorption spectra for (A) RGO, (B) AuNP−RGO, (C) H_2O_2−RGO, and (D) AuNP−H_2O_2−RGO. The solutions were irradiated with water-filtered white light from a Xe lamp for 2 h with UV−visible absorption measurements taken in 10 min intervals. The decrease in absorption over time in panel D is inferred to be RGO oxidation since, commonly, reduction processes in solution lead to increases in absorption. Labels a−m represent individual measurements in 10 min intervals. Inset images are of solutions after 2 h irradiation. AuNP concentration was 20 μM based on [$AuCl_4^-$], and RGO concentration was 0.1 mg/mL.

the material afford 3-D electrode designs that facilitate diffusion of ions through wrinkle-induced tunnels, edges, and macropores.[51−54] Considerable focus has been placed in developing unique morphologies from RGO, including some with micro- and nanoporous facets that exhibit excellent performance as supercapacitor electrodes.[45,55−59] By creating pores within the graphene sheets, the surface area can be increased and improvements in diffusion of electroactive species can be realized. Thus, while graphene itself is a rich and complex material, these newly explored polymorphs exhibit potential for use in opto-electronic and renewable energy applications.

In the present work, we explore the direct and AuNP-catalyzed reaction between RGO and hydroxyl radicals and utilize the reaction to generate a new graphene morphology with nanopores and wrinkles herein referred to as oxidized RGO (ORGO). UV photolysis of H_2O_2 leads to the production of 2OH$^\bullet$ and provides a convenient means to study the reactivity of organics with OH$^\bullet$ radicals. AuNPs are also established aerobic oxidation catalysts[60] and have been shown to create pore-based defects in suspended single-layer graphene sheets.[61] Looking at OH$^\bullet$ radical reactivity toward graphene from the perspective of material applications shows potential challenges with evolution of hydroxyl radicals in energy-related reactions such as TiO_2 photocatalysis[62−64] and fuel cell cathode O_2 reduction.[65,66] Additionally, superoxide radicals evolve during charging of a lithium−oxygen battery, which may lead to graphene degradation when used as a substrate for cathode catalytsts.[67−69] Elucidating the mechanism behind the oxidation of RGO to ORGO provides opportunities to suppress these unwanted reactions in photocatalytic or electrochemical systems containing graphene-based composite materials. Finally, the exploration of OH$^\bullet$ radical oxidation of RGO with and without the catalytic effect of AuNPs can facilitate new methods to tune the optical and electronic properties of RGO by varying the degree of oxidation, functional group selectivity, and/or morphology.

RESULTS AND DISCUSSION

Reactivity of OH$^\bullet$ toward RGO. We subjected chemically reduced RGO to white light irradiation (300 W Xe lamp with quartz water filter) for 2 h with four different suspensions containing RGO, H_2O_2−RGO, AuNP−RGO, and AuNP−H_2O_2−RGO. The UV irradiation of solutions containing H_2O_2 generates highly reactive OH$^\bullet$ radicals. Figure 1 shows the changes in absorption of these four suspensions recorded over the course of the 2 h irradiation time. In general, UV irradiation of GO

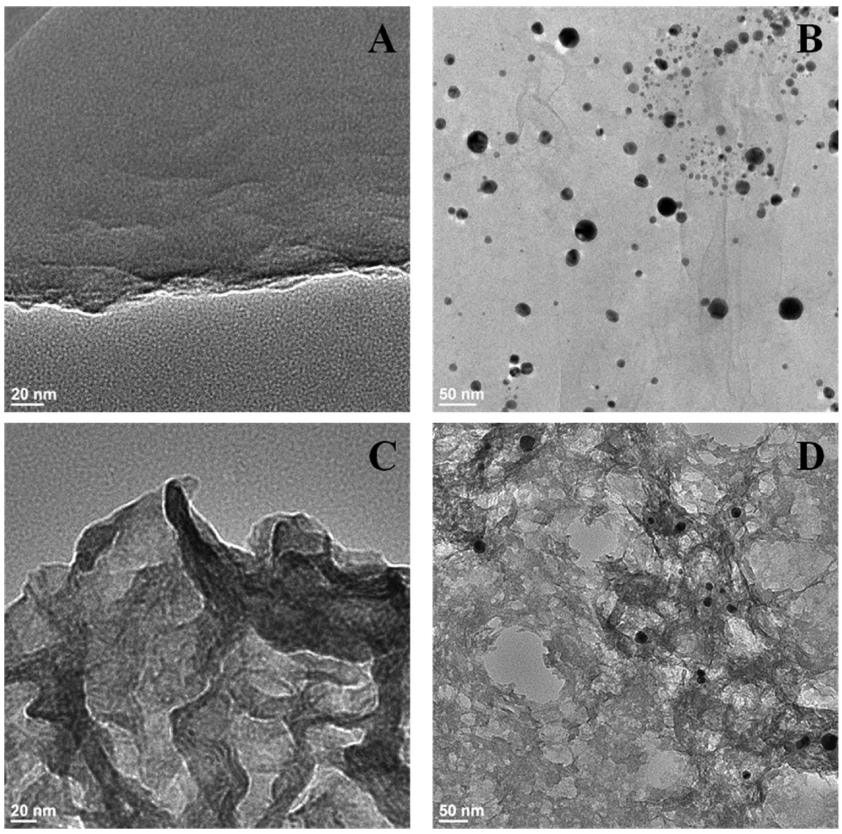

Figure 2. TEM images of (A) RGO, (B) Au + RGO, (C) H_2O_2 + RGO, (D) Au + H_2O_2 + RGO after 2 h irradiation time. The characteristic feature of pores in (D) is unique to the AuNP−H_2O_2 system. However, irradiation with H_2O_2 alone resulted in the wrinkled structure in (C), but no RGO surface changes were observed in (A) and (B).

(or RGO) in aqueous solution leads to photochemical reduction, and the reduction progress can be monitored from the increase in scattered and absorbed light across the UV−visible spectrum (Figure 1A). Accordingly, the solutions without H_2O_2 (Figure 1A,B) exhibit increased visible absorption and scattering, which is in agreement with the UV-assisted reduction of residual GO moieties. In contrast, the inclusion of H_2O_2 and noble metal catalyst, AuNPs, during irradiation leads to consecutive decreases in absorption during the 2 h irradiation (spectra a−m, 10 min intervals in Figure 1D). If the suspension contains only H_2O_2 and RGO during irradiation, both reduction of residual GO and slower oxidation of RGO seem to compete. We observe a small increase in the absorption in the visible region which quickly saturates during the first 50 min (Figure 1C, spectra a−f), thus confirming the reduction process during the initial period of UV irradiation. Small decrease in absorbance seen in the 300−400 nm region after 50 min of irradiation indicates the oxidative role of $OH^{\bullet}$ radicals even without AuNPs.

The photographs of UV-irradiated suspension (see insets in Figure 1) show different degrees of color changes that are visually distinct. While the UV irradiation of GO deepens the color (inset Figure 1A), the presence of H_2O_2 lightens the color (inset Figure 1C). The color change of the AuNP−H_2O_2−RGO suspension in the inset of Figure 1D is dramatically different as the transparency of the solution increased substantially. The residual pink color represents the remaining AuNPs in the suspension. As evidenced from the absorption spectra in Figure 1C, the $OH^{\bullet}$ radicals alone are capable of carrying out only limited changes in RGO, but the absorption changes become significant when AuNPs are present in the RGO suspension (Figure 1D). These observations suggest that the AuNPs serve as catalysts to promote the reaction between $OH^{\bullet}$ and RGO resulting in oxidized RGO or ORGO. Since the Au plasmon peak at 540 nm remains unaffected after UV irradiation with RGO, we can further ascertain the catalytic role of AuNPs in the overall oxidation process. It should be noted that the presence of RGO is important to attain the photostability. If the AuNPs are irradiated with H_2O_2 only, changes in the AuNP absorption spectra are observed. These particles eventually aggregate and crash from suspension (Figure S1 Supporting Information).

The morphology of the irradiated samples was investigated using transmission electron microscopy (TEM). The high-resolution images shown in Figure 2 contrast the resulting surface features of the RGO following irradiation (see Supporting Information Figure S2 for the TEM image of pre-irradiated RGO). Irradiated RGO in Figure 2A shows multilayered sheets as the individual sheets become stacked along the graphitic *c*-axis during

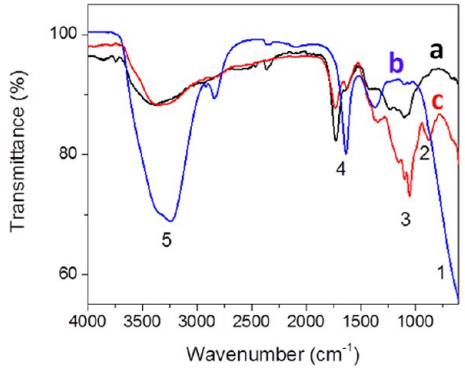

	cm^{-1}	Characteristic
1	500-900	-OH
2	800-1000	C=C-H
3	1000-1250	C-O
4	1700-1750	C=O
5	3000-3700	-OH

Figure 3. FTIR spectra of (a) 2 h irradiated AuNP−H_2O_2−RGO, (b) 2 h irradiated H_2O_2−RGO, and (c) pre-irradiated RGO. The table identifies relevant functionalities with the observed IR absorption modes. Significant −OH stretching builds into the absorption characteristics of the direct OH$^•$ radical attack relative to the AuNP-assisted reaction. AuNPs catalyze further oxidative processes beyond the initial −OH addition.

UV irradiation. On the other hand, the sample with RGO and AuNPs in Figure 2B exists as a single- to few-layer form following UV irradiation. As discussed earlier,[70] binding with AuNPs prevents stacking of individual layers and thus renders sustained exfoliation of the individual RGO sheets. The RGO irradiated with only H_2O_2 in Figure 2C exhibits significant wrinkling after irradiation with H_2O_2, whereas RGO irradiated with H_2O_2 and AuNPs exhibits both wrinkles and 5−100 nm diameter pores (Figure 2D). The surface wrinkling effect is seen in the irradiation experiments where H_2O_2 was included. The decomposition of H_2O_2 to H_2O and O_2 is a competing reaction with hydroxyl radical production during irradiation. The wrinkling effect observed across the ORGO sheets arises from O_2 bubble nucleation on the RGO surface. However, the presence of Au nanoparticles accelerates RGO oxidation as evident from the formation of nanopores. This Au-mediated oxidation results in the formation of ORGO, rendering a "*Holey Graphene*" morphology. It is evident that these nanosize pores represent complete oxidation of C═C network in the immediate vicinity of metal nanoparticles.

FTIR spectroscopy was used to probe the chemical changes of the ORGO through the OH$^•$ radical reaction. The FTIR spectra shown in Figure 3 indicate C═C attack by OH$^•$ yielding higher absorption in the regions of −OH and C═O modes and lower absorption in the regions of various C═C−H and C−O modes for the resulting ORGO. The spectra of the post-irradiated (a) AuNP−H_2O_2−RGO and (b) H_2O_2−RGO samples and (c) pre-irradiated RGO highlight the differences in the resulting chemical structure of the ORGO when AuNPs are introduced in the suspension. While the FTIR spectrum of RGO is inherently rich with various absorption characteristics, the drastic changes following the 2 h irradiation provide insight into the direct and AuNP-mediated OH$^•$ attack on the RGO.

All irradiated samples (2 h) show a decrease in the IR absorption in region 2, corresponding to C═C−H modes of the RGO. A separate 2 h irradiation experiment using GO rather than RGO as precursor with AuNPs and H_2O_2 was conducted to confirm the C═C attack by OH$^•$ since the degree of C═C bonding in GO *versus* RGO is substantially different. The changes in absorbance of the suspension were tracked, and the spectra indicate that some reduction of GO to RGO (*i.e.*, restoration of some degree of C═C bonding) must occur before decreases in absorbance are observed (Supporting Information Figure S3). We also made an attempt to directly oxidize graphite using UV photolysis of H_2O_2, but the lack of significant dispersion of graphite powder in water and the inability of the OH$^•$ radicals to penetrate and exfoliate the graphene layers prevented any significant and observable reaction. Thus, initial exfoliation of graphene layers is important to pursue the OH$^•$ radical reaction and generate ORGO.

The pre-irradiated sample (Figure 3, spectrum c) exhibited a stronger IR absorption by C−O modes in region 3 as compared to the sample after irradiation, but both irradiated samples show increases in C═O modes in region 4. The absorption of the post-irradiated H_2O_2−RGO sample in region 4 (Figure 3, spectrum b) is shifted slightly to lower wavenumber relative to the AuNP−H_2O_2−RGO sample (Figure 3, spectrum a). This shift is attributed to the differences in the localized surface functionalities resulting from the variation in the oxidative reaction mechanism induced by AuNPs. The most striking contrast is observed in the H_2O_2−RGO spectrum with the large growth of the two broad −OH absorption bands in regions 1 and 5, compared with only a slight increase in −OH absorption in the AuNP−H_2O_2−RGO spectrum. This observation implies that the AuNPs alleviate a buildup of −OH groups on the RGO sheets by providing a pathway for further oxidation. The formation of holey graphene sheets is in support of the argument that AuNPs catalyze the oxidation reaction to CO_2.

Establishing the Catalytic Role of AuNPs in RGO Oxidation. There are two possible reaction pathways with which Au nanoparticles could catalyze the RGO oxidation: (1) to promote photolytic OH$^•$ formation *via* UV photolysis of H_2O_2, thus resulting in higher OH$^•$ radical concentrations near the AuNP surface, and (2) to promote the reaction between OH$^•$ and RGO aided by the changes in the

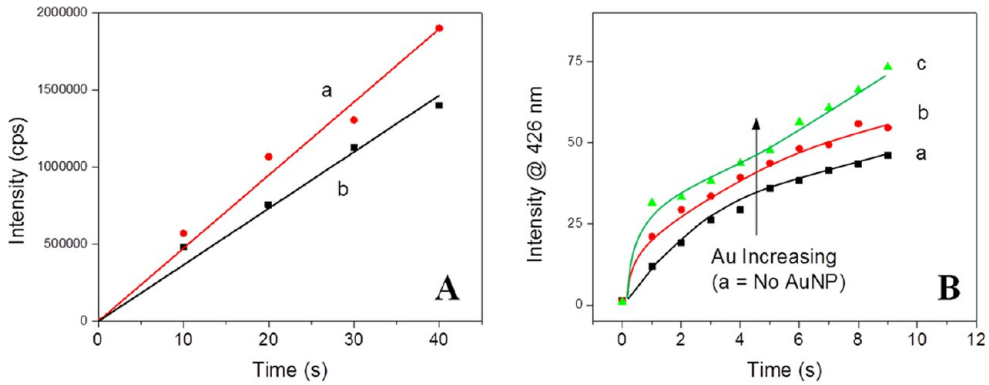

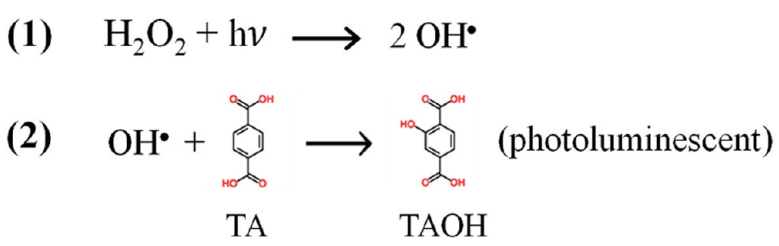

Figure 4. (A) Fluorescence intensity of TAOH measured at 426 nm after each 10 s irradiation interval: (a) 0.3 M H_2O_2 with 15 μM AuNP (based on [$AuCl_4^-$] precursor) and (b) 0.3 M H_2O_2 without AuNP. (B) Fluorescence intensity monitored continuously at 426 nm during UV irradiation of 0.3 M H_2O_2 solution: (a) 0 μM, (b) 3 μM, and (c) 6 μM AuNP (based on [$AuCl_4^-$] precursor). The higher fluorescent counts when AuNPs are present during the photolysis indicate a catalytic effect for $OH^\bullet$ radical formation *via* H_2O_2 photolysis. Lines in panel B do not represent fits and are drawn to depict the trend.

localized oxidation potentials at the AuNP surface. In particular, the catalytic process (2) is facilitated by the fact that AuNPs are bound to the RGO.

We first monitored the conversion of terephthalic acid (TA) into 2-hydroxyterphthalic acid (TAOH) to establish the production of the $OH^\bullet$ radical during the steady-state illumination experiments. Aqueous TA reacts irreversibly with $OH^\bullet$ to form fluorescent TAOH (Figure 4). TAOH exhibits strong fluorescence at 426 nm under UV excitation and has been used to monitor hydroxyl radical detection in photochemical and photocatalytic experiments.[71−73] Figure 4A shows an increase in fluorescence intensity at 426 nm during the irradiation of TA solution in the presence of AuNPs. Fluorescence measurements were collected after discrete 10 s intervals of irradiation (Figure 4A). The observed increase in fluorescence intensity during illumination is reflective of increased production of $OH^\bullet$ radicals as the concentration of TAOH is proportional to the overall production of $OH^\bullet$ radicals. By calculating the linear slope of the discrete points in Figure 4A and assuming a linear relationship between fluorescence intensity and [TAOH], it is found that the AuNP-catalyzed photolysis generated ~30% more hydroxyl radicals in this time frame (slope ratio = 1.3).

We also continuously monitored the emission intensity at 426 nm during UV irradiation using an Ocean Optics fiber optics enabled spectrometer in intensity mode to gauge incremental additions of AuNPs to the TA solution during steady-state illumination. The abundant UV source of photolysis with a Xe lamp is sufficient to excite TAOH, and its emission can be captured through a fiber optic bundle attached to the cell at 90° to the illumination path. The increase in intensity captured during first 10 s of irradiation shows a dependence on the amount of AuNPs present in the solution. The increased fluorescence of TAOH with increased AuNP concentration is attributed to increased production of the $OH^\bullet$ radical. This finding further ascertains the role of AuNPs in catalyzing the UV photolysis of H_2O_2.

Next, we wanted to establish the reactivity of RGO with $OH^\bullet$ radicals and see how this reactivity is influenced by the presence of AuNPs. We performed nanosecond laser flash photolysis experiments using the fourth harmonic (266 nm) of a Nd:YAG laser as the excitation source to generate $OH^\bullet$ radicals and follow the course of the reaction with transient absorption spectroscopy. Since the $OH^\bullet$ radical does not provide absorption for direct monitoring in the visible, we monitored the formation of $(SCN)_2^{-\bullet}$ radicals by reacting SCN^- with $OH^\bullet$ radicals. As has been established in the pulse radiolysis reaction of the $OH^\bullet$ radical with SCN^-, this reaction results in quantitative production of $(SCN)_2^{-\bullet}$ radicals (λ_{max} = 475 nm, ε_{475} = 7600 M^{-1} cm^{-1}).[74] If another species (*viz.*, RGO in the present case) is present in the solution to compete for $OH^\bullet$ radicals, it is possible to obtain the kinetic details of its reactivity using competition kinetics analysis.

In the present experiment, $(SCN)_2^{-\bullet}$ radical quantum yields were determined by monitoring ΔAbs at 475 nm in the presence and absence of RGO. $(SCN)_2^{-\bullet}$ radicals were generated photolytically *via* reaction of SCN^- with $OH^\bullet$ radicals produced using 266 nm laser

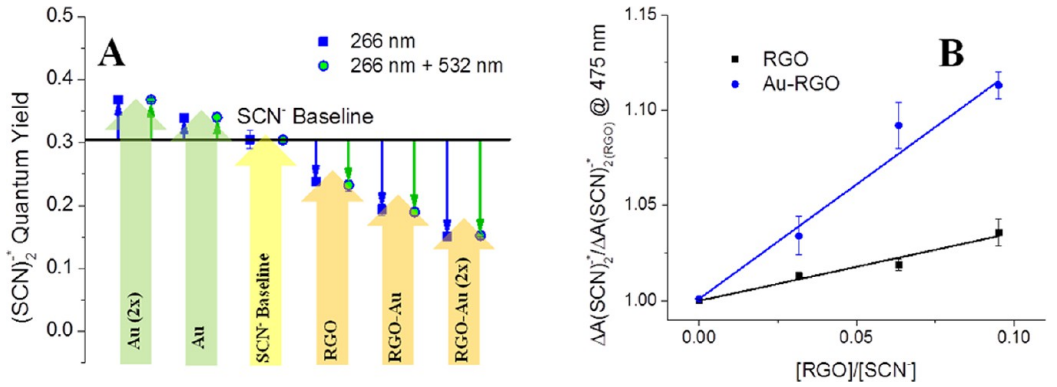

Figure 5. Laser flash photolysis and competition kinetics were used to evaluate the quantum yield of thiocyanate radical generation from H_2O_2 photolysis and the rate constants for catalyzed and direct $OH^•$ attack on RGO, respectively. Points above the $(SCN)_2^{-•}$ baseline in panel A represent AuNP-catalyzed production of $OH^•$; those below represent competitive scavenging of $OH^•$ by RGO. Experiment: AuNP 2× (15 μM based on $[AuCl_4^-]$), AuNP (7.5 μM), baseline (4 μM SCN^-), RGO (0.13 μM based on estimated reduced carbon in RGO), RGO (0.13 μM) + AuNP (7.5 μM), RGO (0.13 μM) + Au NP 2× (15 μM). Panel B shows the linear trends resulting from second-order kinetics when the ratios of peak yield of thiocyanate radicals without RGO to that with RGO are plotted with respect to reactant concentration ratios. Error bars represent standard deviation of trials ($n \geq 3$ for each concentration ratio).

pulse irradiation of H_2O_2.[75] Additional experiments were performed with AuNPs only to further gauge the catalytic influence of AuNPs on the photolysis of H_2O_2 and validate the TAOH fluorescence data discussed in Figure 4. The summary of the flash photolysis results expressed in terms of the $(SCN)_2^{-•}$ quantum yields measured in the absence and presence of AuNPs and RGO is presented in Figure 5A. The $(SCN)_2^{-•}$ yield increases with increasing concentration of AuNPs, which reflects greater production of $OH^•$ radicals. The decrease in $(SCN)_2^{-•}$ yield when RGO was present reflects the competition between SCN^- and RGO to capture $OH^•$ radicals. The $(SCN)_2^{-•}$ quantum yield (0.305) measured in the absence of any competitive species serves as a baseline for comparison (represented by the horizontal line).

Of particular interest is the substantial decrease in $(SCN)_2^{-•}$ yield seen when AuNPs are present in the solution along with RGO. The lower yield of $(SCN)_2^{-•}$ is indicative of the fact that the $OH^•$ radicals are competitively consumed during RGO oxidation. The higher reactivity of $OH^•$ radicals toward RGO when AuNPs are present contrasts the higher $(SCN)_2^{-•}$ yield observed when AuNPs are in suspension without RGO. To determine whether this reactivity is influenced by the absorption of light by the AuNPs, we introduced a second simultaneous laser pulse (532 nm) in the excitation path so that the localized surface plasmon resonance of AuNPs could be selectively activated. When this second pulse (532 nm) was introduced along with 266 nm excitation pulse, no statistically significant differences for $(SCN)_2^{-•}$ quantum yield could be seen (Figure 5A). Even at longer continuous pulsed irradiation times (30 min) with single- and double-beam excitation, the difference observed in the changes in the UV−visible absorption of the samples was small (Supporting Information Figure S4).

Plasmon resonance in AuNPs is known to produce significant localized heating in irradiated aqueous solutions with plasmon excitation.[76] We measured the steady-state temperature of a suspension of AuNPs and of the same volume of water after 10 min of white light irradiation and found a 20 K increase above ambient when AuNPs were present compared to 13 K increase in the solutions without AuNPs. Although thermal effects arise from the surface plasmon excitation of AuNPs, we find that these effects are not the major contributors to the $OH^•$ radical-induced oxidation. The nanosecond laser flash photolysis conclusively demonstrates the role of AuNPs primarily to be catalytic.

We further analyzed the reactivity of RGO toward $OH^•$ radicals by varying the ratio of RGO to SCN^- in the suspension with and without AuNPs. This procedure allowed us to evaluate and compare the rate constants associated with $OH^•$ radical attack on RGO with and without AuNPs using a second-order kinetics model. Figure 5B shows the changes in $(SCN)_2^{-•}$ yield with variations in [RGO] for calculation of rate constants with and without AuNPs. We have converted RGO concentration in terms of molar carbon with the assumption that RGO has a C/O ratio of 15, which has been reported for borohydride reduction of GO.[30] The reactions of interest in the competition kinetics experiments are shown below as reactions 1−3. Since the SCN^- and RGO are in "competition" for the $OH^•$ radicals, knowing the rate of $OH^•$ radical reaction with thiocyanate ions enables calculation of the competitor rate constant, in this case RGO.

$$H_2O_2 + h\upsilon \rightarrow 2OH^• \quad k_{photolysis} \tag{1}$$

$$OH^• + 2SCN^- \rightarrow (SCN)_2^{-•} + OH^- \quad k_{SCN^-} \tag{2}$$

$$OH^• + RGO \rightarrow ORGO \quad k_{RGO} \tag{3}$$

The final relationship between $(SCN)_2^{-•}$ yield with and without RGO is given in eq 4. The ratios of the $(SCN)_2^{-•}$ yields are plotted against the ratio of [RGO] to

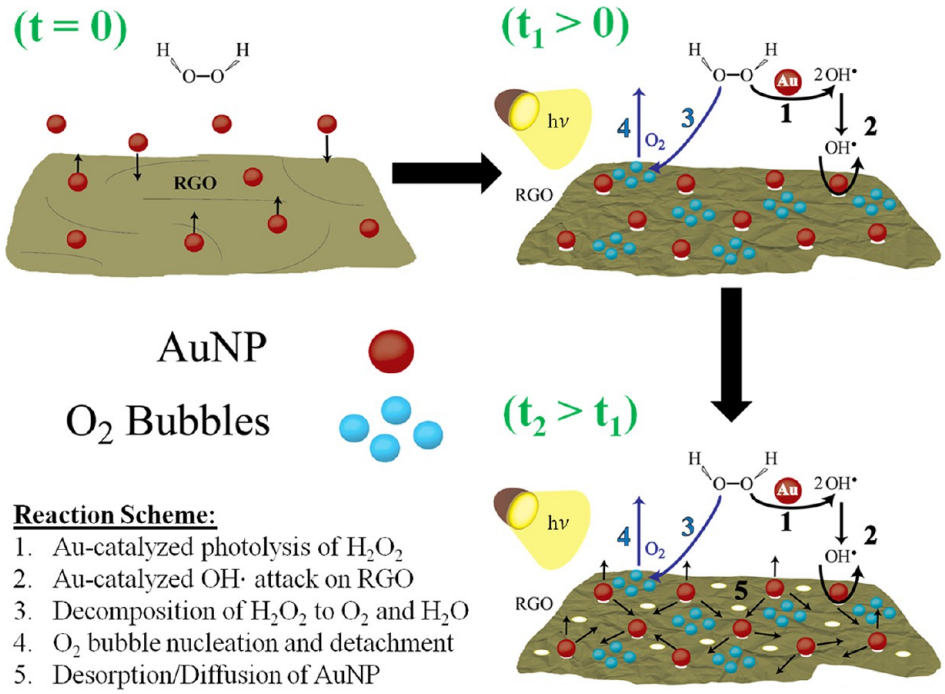

Scheme 1. Proposed mechanism for the photoinduced reaction between RGO, AuNPs, and H_2O_2. A suspension of RGO, AuNPs, and H_2O_2 is prepared as shown at $t = 0$. Upon irradiation, AuNPs catalyze photolytic production of $OH^•$ as well as $OH^•$ attack on RGO. Competitive decomposition of H_2O_2 to O_2 leads to bubble nucleation and detachment from the RGO surface, to which we attribute the observed wrinkling of the RGO sheets. Extended irradiation leads to migration of AuNPs and creation of nanopores at various places along the RGO sheets through diffusion and/or adsorption/desorption.

$[SCN^-]$, and the slope is proportional to the ratio of the competitor rate constants (*e.g.*, RGO and SCN^-). Details of competition kinetics modeling, estimation of rate constants, and other experimental details are presented in the Supporting Information.

$$\frac{\Delta A_{475nm}(SCN)_2^{-\bullet}}{\Delta A_{475nm}(SCN)_2^{-\bullet}RGO} = \left(\frac{k_1[RGO]}{k_2[SCN^-]} + 1\right)\frac{[OH^\bullet]_0}{[OH^\bullet]_{0,\,RGO}} \quad (4)$$

By varying [RGO] with and without AuNPs, the rate constants for $OH^•$ attack on RGO were calculated from the slope of the linear plots in Figure 5B using the rate constant for the formation of thiocyanate radical from $OH^•$, which is reported as $k_{(SCN)2}{}^{-\bullet} = 1.3 \times 10^{10}\ M^{-1}\ s^{-1}$.[75] Using this value, the rate constants for direct and AuNP-catalyzed $OH^•$ reaction with RGO are calculated as $k_{RGO} = 4.4 \times 10^9\ M^{-1}\ s^{-1}$ and $k_{Au\text{-}RGO} = 1.2 \times 10^{10}\ M^{-1}\ s^{-1}$. The ratio of the Au-catalyzed and direct rate constants shows that the AuNPs increase the kinetics of the reaction by a factor of 2.7. It should be noted that both catalytic roles of AuNPs in the $OH^•$ radical production and $OH^•$ radical attack on RGO are convoluted in the $(SCN)_2{}^{-\bullet}$ quantum yield when AuNPs and RGO are present together in the solution. For example, the average ratio of the $(SCN)_2{}^{-\bullet}$ quantum yield measured with 2 × [AuNP] (*viz.*, 15 μM) and the baseline quantum yield (*viz.*, no AuNP) in Figure 5A,B is 1.29 ± 0.048. This value is in agreement with the value of 1.3 obtained *via* ratio of slopes in Figure 4A. The rate-limiting step in the overall reaction is that of the $OH^•$ radical attack on RGO. Although AuNPs catalyze production of $OH^•$ radicals, reaction 1 listed above occurs instantaneously relative to the pulse width (10 ns) of the nanosecond laser.[75] Any acceleration of $OH^•$ radical production from AuNPs will not influence the overall rate of $OH^•$ radical attack on RGO.

Proposed Mechanism and Reaction Modulation. The morphological changes initiated by the photolysis of H_2O_2 show two distinct phenomena: (1) the initial wrinkling of RGO sheets followed by (2) the AuNP-induced hole creation. The mechanism of the photoinduced conversion of RGO to ORGO is illustrated in Scheme 1. At t = 0 min, a suspension of RGO, AuNPs, and H_2O_2 exists in equilibrium (AuNP adsorption−desorption, H_2O_2−RGO surface interactions, AuNP−H_2O_2 surface interactions). This equilibrium is disturbed upon irradiation with UV light ($t_1 > 0$), resulting in the initiation of a variety of physical and chemical transformations. These processes, labeled 1−4 in Scheme 1, are (1) Au-catalyzed photolysis of H_2O_2, (2) Au-mediated $OH^•$ attack on RGO, (3) diffusion of H_2O_2 and decomposition at the RGO surface, and (4) O_2 evolution associated with nucleation and bubble formation on the RGO surface. As time progresses ($t_2 > t_1$), the AuNPs diffuse across the RGO and adsorb−desorb from various points on the surface (5), creating new nanopores at different locations along the ORGO sheets. On the basis of Figure 2C,D, it is apparent that the wrinkling of the RGO sheets can be attributed to rapid nucleation of O_2 bubbles on the surface (process 4).

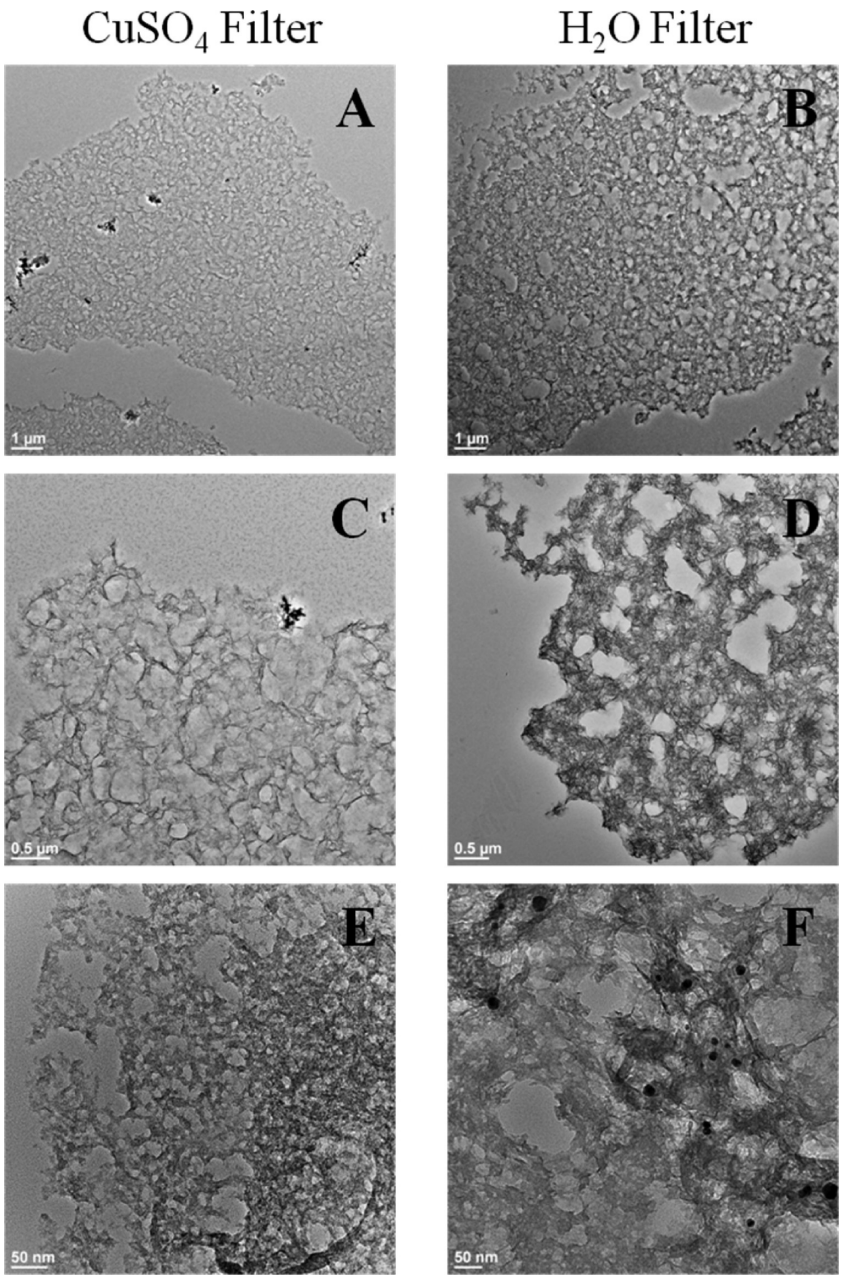

Figure 6. TEM micrographs showing ORGO produced with water-filtered white light (A,C,E) and with $CuSO_4$-filtered white light (B,D,F). Water filters only infrared light. The filtering of UV−B and UV−C photons (>290 nm) by $CuSO_4$ further reduces the UV photons for the decomposition of H_2O_2, thus leading to fewer $OH^•$ radicals available for reaction with RGO. The wrinkles and larger pores seen in the water-filtered ORGO synthesis were noticeably significant (see, for example, B *vs* A and D *vs* C).

The hydroxyl-mediated oxidation of aromatic molecules has long been established.[77] The initial attack of $OH^•$ radical produces an OH adduct or undergoes electron transfer to produce cation radicals. Continued attack of hydroxyl radicals causes complete oxidation of the organic compounds to CO_2 and water. In fact, the hydroxyl-mediated mineralization of organic compounds has been the basis of TiO_2-assisted photocatalysis and other advanced oxidation processes.[78] The presence of AuNPs on the RGO surface catalyzes this oxidation, creating pores. As a single AuNP becomes detached, it moves to another nascent site to induce additional pores. By modulating the light intensity, wavelength of excitation, and time of exposure, it should be possible to control the morphology of ORGO.

We attempted to modulate the ORGO morphology and/or pore structure through selective control of the incident photon flux *via* light filtering. Two sets of experiments were performed. In the first set, a water filter was introduced to decrease the IR photons reaching the sample. In the second set, we replaced the water with a $CuSO_4$ solution. $CuSO_4$ filters UV−B and UV−C photons (<290 nm), thus limiting energetic

photons arriving at the sample, particularly in the photolytic range of interest (200−300 nm photons are responsible for efficient photolysis of H_2O_2) and in the visible and NIR (>650 nm). Absorption spectra of water and $CuSO_4$ are shown in Figure S5 of Supporting Information. Limiting the excitation range provides a means to reduce the rate with which $OH^•$ radicals are produced. The filtering of UV photons decreased the average size of the pores and the wrinkling intensity in the ORGO sheets as seen in the TEM image array in Figure 6 (wrinkles exhibit stronger contrast in the RGO TEM images). As the steady-state concentration of hydroxyl radicals is decreased, we observe the morphology of the ORGO to be altered through reduction of pore size and wrinkling features.

CONCLUSIONS

Perspectives on *Holey* Graphene. Through the Au-catalyzed $OH^•$ radical attack of RGO, a new graphene-based material, which we refer to as *Holey Graphene* or ORGO, with nanopores and wrinkles can be generated. AuNPs act as multifunctional catalysts that increase the $OH^•$ radical yield from UV photolysis of H_2O_2 and mediate the reaction between $OH^•$ radicals and RGO. While the AuNPs are responsible for the development of the pore structure, the $OH^•$ radicals attack RGO directly and build significant numbers of −OH functionalities on the ORGO sheet as observed in FTIR spectra. Hydroxyl radical driven reaction can facilitate production of new graphene materials whose properties (*i.e.*, degree of oxidation, nanoporous structure) can be tuned toward specific applications. This work complements recent advances in theoretical understanding of various functionalities of the RGO and/or GO surface chemistry and their influence on the work function.[79]

The results presented here also enable understanding of RGO stability when used in applications where free radical formation would be expected (*e.g.*, photocatalysis or electrocatalysis). For example, graphene-supported metal nanoparticles have recently been proposed as superior fuel cell catalysts or for photocatalysis.[80−82] However, the undesirable cathodic side reaction in a H_2/O_2 fuel cell is the formation of $OH^•$ radicals.[83,84] When such reaction occurs in a fuel cell, even with a low probability, it could lead to increased degradation of carbon support (*viz.*, graphene). The same applies to photocatalytic systems involving graphene-supported TiO_2 since the dominant oxidation pathway in aqueous TiO_2 photocatalysis is evolution of $OH^•$ radicals from trapped holes on the TiO_2 surface.[62−64] Most of these studies are conducted under short-term operation without probing the stability of the RGO support. Hence, caution should be exercised while employing graphene-based metal composites as catalysts in energy conversion processes. The present study implies that the $OH^•$ radical attack on graphene-based supports cannot be ignored. On the other hand, holey graphene may be a better support to design Li-ion storage batteries or other electrochemical devices where diffusion of dissolved electroactive species strongly influences the device performance.

EXPERIMENTAL SECTION

ORGO Synthesis and Materials. GO was synthesized using a modified Hummers method.[25] In short, 2 g of graphite powder was sonicated and stirred in an ice bath in 92 mL of concentrated H_2SO_4 (Fisher 99%) with 2 g of $NaNO_3$ (Aldrich 99%) for 30 min, after which 12 g of $KMnO_4$ (Aldrich 99%) was very slowly added. Sonication continued for 30 min following addition of $KMnO_4$, after which the flask was removed and allowed to stir slowly overnight at 30 °C. Next, 100 mL of deionized (DI) H_2O was added dropwise under nitrogen sparging followed by 1 h of stirring. Finally, 600 mL of 3% H_2O_2 (Fisher, 30%) was dispensed into the flask, yielding a yellowish-brown GO suspension. The suspension was washed three times with concentrated HCl *via* settling and resuspension, three times with 1 M HCl *via* centrifuge, and finally five times with DI H_2O. RGO was synthesized by adding 10 mM $NaBH_4$ (Aldrich 99%) to a 0.2 mg/mL suspension of GO. Few flocculants settled, and the suspended sheets in the supernatant were retained for use.

Au nanoparticles were synthesized by preparing an aqueous solution containing 200 μM $HAuCl_4$ (Sigma 99.99%) and 200 μM anhydrous trisodium citrate (Fisher 99%). $NaBH_4$ solution (2 mM) was then added directly to the vial while stirring vigorously. The solution turned black, then almost immediately turned deep reddish purple and remained stable on the lab bench. Sufficient time for residual borohydride reaction was afforded before use of the RGO in experiments. A 1 cm quartz cuvette was used for fluorescence and photolysis experiments. Terephthalic acid (Sigma 99%) was used to make 0.1 M stock in 0.1 M NaOH, and 0.1 mM solutions were used in fluorescence experiments. In a typical photolysis experiment, 2.6 mL of RGO solution, 100 μL of 30% H_2O_2, and 300 μL of AuNPs were added to the cuvette. A 300 W Xe lamp was used with the cuvette positioned 12 in. from the light source for high intensity irradiation. A 2 in. cube quartz filter was used with water and a copper sulfate solution (0.05 M, Sigma 99%) for light filtering experiments.

ORGO Characterization. UV−visible absorption spectra were recorded with a Varian UV−visible spectrophotometer. TEM images were obtained using Titan 80-300 300 kV electron microscope. TEM grids were prepared by drop-casting followed by drying under a heat lamp for 10 min and finally in vacuum for 24 h. FTIR spectra were recorded with a Shimadzu IR Prestige-21 FTIR, and the spectra represent the average of 20 scans. The discrete fluorescence measurements were taken using a Fluorolog emission spectrometer after each of six intervals of 10 s irradiation, and the real-time fluorescence counts were measured with an Ocean Optics detector system with a white light excitation source (same setup as photolysis experiments). The concentration of AuNPs was reduced for the terephthalic acid experiments to minimize any scattering effects the AuNPs would have on the observed fluorescence measurements. Scattering was corrected by adding AuNPs to the final TAOH solution in the discrete measurements after the sixth 10 s irradiation interval and determining the percentage decrease in fluorescence yield (less than 5% at concentrations tested).

Nanosecond Flash Photolysis Experiments. The nanosecond laser flash photolysis experiments were carried out using a Spectra-Physics Nd:YAG laser system. The 266 nm (fourth harmonic) and 532 nm (second harmonic) pulsed beams were used in photolysis of H_2O_2 and excitation of Au plasmon, respectively. Laser excitation of the sample was at a right angle relative to the monitoring white light beam. Potassium thiocyanate (Aldrich 99%) was used as the thiocyanate source for competition kinetics and measurement of primary quantum yield of

$(SCN)_2^{-\bullet}$. Transient spectra of thiocyanate radical yield were recorded at 475 nm, and an average of three measurements was used for each trial. An average of five trials was recorded for each experimental variation, and statistical significance was calculated at $p < 0.05$. The detection system consisted of a 1000 W Xe lamp as white light source and Spex 270 M monochromator connected to a Hamamatsu R955 photomultiplier. The photomultiplier response was recorded by a LeCroy 7200 digital oscilloscope connected to a PC-AT compatible computer. Double-beam experiments consisting of 266 and 532 nm excitation sources were accommodated using mirror optics for the 532 nm beam. Slight path length differences were necessary, but the delay time was less than the detection limits of the system. The energy of the 266 nm beam was 10 mJ/pulse, and the 532 nm beam was 15 mJ/pulse. Thiocyanate quantum yield was calculated using a naphthalene actinometer ($\varepsilon_{(triplet,414\ nm)} = 14400\ M^{-1}\ cm^{-1}$, $\Phi_{triplet} = 0.75$) with 266 nm excitation.

Conflict of Interest: The authors declare no competing financial interest.

Acknowledgment. This work was supported by the U.S. Army TARDEC under Contract No. W56HZV-08-C-0236, through a subcontract with Mississippi State University, and was performed as part of the Simulation Based Reliability and Safety (SimBRS) research program. As the authors are not government employees, this document was only reviewed by the U.S. government for export controls and improper Army association or emblem usage considerations. All other legal considerations are the responsibility of the author and their employer. P.V.K. acknowledges the support of by the Division of Chemical Sciences, Geosciences, and Biosciences, Office of Basic Energy Sciences of the U.S. Department of Energy through Award DE-FC02-04ER15533. This is contribution number NDRL 4970 from the Notre Dame Radiation Laboratory. We thank Dr. Gordon Hug for assistance in flash photolysis experiments and interpretation of the results.

Supporting Information Available: AuNP spectra pre- and post-irradiation without RGO, TEM image of preirradiated RGO, AuNP−H_2O_2−GO absorbance spectra, pre- and post-absorption spectra for extended single- and double-beam laser irradiation of AuNP−H_2O_2−RGO, additional experimental and calculation details for quantum yields and rate constants, and absorption spectra for water and $CuSO_4$ solution are included in the Supporting Information. This material is available free of charge *via* the Internet at http://pubs.acs.org.

REFERENCES AND NOTES

1. Bolotin, K. I.; Sikes, K. J.; Jiang, Z.; Klima, M.; Fudenberg, G.; Hone, J.; Kim, P.; Stormer, H. L. Ultrahigh Electron Mobility in Suspended Graphene. *Solid State Commun.* **2008**, *146*, 351–355.
2. Morozov, S. V.; Novoselov, K. S.; Katsnelson, M. I.; Schedin, F.; Elias, D. C.; Jaszczak, J. A.; Geim, A. K. Giant Intrinsic Carrier Mobilities in Graphene and Its Bilayer. *Phys. Rev. Lett.* **2008**, 100.
3. Li, X. S.; Cai, W. W.; An, J. H.; Kim, S.; Nah, J.; Yang, D. X.; Piner, R.; Velamakanni, A.; Jung, I.; Tutuc, E.; *et al.* Large-Area Synthesis of High-Quality and Uniform Graphene Films on Copper Foils. *Science* **2009**, *324*, 1312–1314.
4. Zeller, P.; Danhardt, S.; Gsell, S.; Schreck, M.; Winterlin, J. Scalable Synthesis of Graphene on Single Crystal Ir(111) Films. *Surf. Sci.* **2012**, *606*, 1475–1480.
5. Yan, Z.; Lin, J.; Peng, Z. W.; Sun, Z. Z.; Zhu, Y.; Li, L.; Xiang, C. S.; Samuel, E. L.; Kittrell, C.; Tour, J. M. Toward the Synthesis of Wafer-Scale Single-Crystal Graphene on Copper Foils. *ACS Nano* **2012**, *6*, 9110–9117.
6. Wang, H.; Wang, G. Z.; Bao, P. F.; Yang, S. L.; Zhu, W.; Xie, X.; Zhang, W. J. Controllable Synthesis of Submillimeter Single-Crystal Monolayer Graphene Domains on Copper Foils by Suppressing Nucleation. *J. Am. Chem. Soc.* **2012**, *134*, 3627–3630.
7. Hamilton, C. E.; Lomeda, J. R.; Sun, Z. Z.; Tour, J. M.; Barron, A. R. High-Yield Organic Dispersions of Unfunctionalized Graphene. *Nano Lett.* **2009**, *9*, 3460–3462.
8. Oh, S. Y.; Kim, S. H.; Chi, Y. S.; Kang, T. J. Fabrication of Oxide-Free Graphene Suspension and Transparent Thin Films Using Amide Solvent and Thermal Treatment. *Appl. Surf. Sci.* **2012**, *258*, 8837–8844.
9. Chen, N.; Liu, Y. T.; Xie, X. M.; Ye, X. Y.; Feng, X.; Chen, Y. F.; Wang, Y. H. High-Concentration Aliphatic and Aromatic Dispersions of Single- and Few-Layer Graphene Noncovalently Modified by Block Copolymer Crystallization. *Carbon* **2012**, *50*, 4760–4764.
10. Skaltsas, T.; Karousis, N.; Yan, H. J.; Wang, C. R.; Pispas, S.; Tagmatarchis, N. Graphene Exfoliation in Organic Solvents and Switching Solubility in Aqueous Media with the Aid of Amphiphilic Block Copolymers. *J. Mater. Chem.* **2012**, *22*, 21507–21512.
11. Hummers, W. S.; Offeman, R. E. Preparation of Graphitic Oxide. *J. Am. Chem. Soc.* **1958**, *80*, 1339–1339.
12. Kim, J.; Cote, L. J.; Kim, F.; Yuan, W.; Shull, K. R.; Huang, J. X. Graphene Oxide Sheets at Interfaces. *J. Am. Chem. Soc.* **2010**, *132*, 8180–8186.
13. Paredes, J. I.; Villar-Rodil, S.; Martinez-Alonso, A.; Tascon, J. M. D. Graphene Oxide Dispersions in Organic Solvents. *Langmuir* **2008**, *24*, 10560–10564.
14. Acik, M.; Lee, G.; Mattevi, C.; Pirkle, A.; Wallace, R. M.; Chowalla, M.; Cho, K.; Chabal, Y. The Role of Oxygen during Thermal Reduction of Graphene Oxide Studied by Infrared Absorption Spectroscopy. *J. Phys. Chem. C* **2011**, *115*, 19761–19781.
15. Larciprete, R.; Fabris, S.; Sun, T.; Lacovig, P.; Baraldi, A.; Lizzit, S. Dual Path Mechanism in the Thermal Reduction of Graphene Oxide. *J. Am. Chem. Soc.* **2011**, *133*, 17315–17321.
16. Stankovich, S.; Dikin, D. A.; Piner, R. D.; Kohlhaas, K. A.; Kleinhammes, A.; Jia, Y.; Wu, Y.; Nguyen, S. T.; Ruoff, R. S. Synthesis of Graphene-Based Nanosheets *via* Chemical Reduction of Exfoliated Graphite Oxide. *Carbon* **2007**, *45*, 1558–1565.
17. Gomez-Navarro, C.; Weitz, R. T.; Bittner, A. M.; Scolari, M.; Mews, A.; Burghard, M.; Kern, K. Electronic Transport Properties of Individual Chemically Reduced Graphene Oxide Sheets. *Nano Lett.* **2007**, *7*, 3499–3503.
18. Gilje, S.; Han, S.; Wang, M.; Wang, K. L.; Kaner, R. B. A Chemical Route to Graphene for Device Applications. *Nano Lett.* **2007**, *7*, 3394–3398.
19. Shao, Y. Y.; Wang, J.; Engelhard, M.; Wang, C. M.; Lin, Y. H. Facile and Controllable Electrochemical Reduction of Graphene Oxide and Its Applications. *J. Mater. Chem.* **2009**, *20*, 743–748.
20. Ramesha, G. K.; Sampath, S. Electrochemical Reduction of Oriented Graphene Oxide Films: An *In Situ* Raman Spectroelectrochemical Study. *J. Phys. Chem. C* **2009**, *113*, 7985–7989.
21. Guo, H. L.; Wang, X. F.; Qian, Q. Y.; Wang, F. B.; Xia, X. H. A Green Approach to the Synthesis of Graphene Nanosheets. *ACS Nano* **2009**, *3*, 2653–2659.
22. Yu, H. W.; He, J. J.; Sun, L.; Tanaka, S.; Fugetsu, B. Influence of the Electrochemical Reduction Process on the Performance of Graphene-Based Capacitors. *Carbon* **2013**, *51*, 94–101.
23. Yang, J.; Gunasekaran, S. Electrochemically Reduced Graphene Oxide Sheets for Use in High Performance Supercapacitors. *Carbon* **2013**, *51*, 36–44.
24. Williams, G.; Seger, B.; Kamat, P. V. TiO_2-Graphene Nanocomposites. UV-Assisted Photocatalytic Reduction of Graphene Oxide. *ACS Nano* **2008**, *2*, 1487–1491.
25. Lightcap, I. V.; Kosel, T. H.; Kamat, P. V. Anchoring Semiconductor and Metal Nanoparticles on a Two-Dimensional Catalyst Mat. Storing and Shuttling Electrons with Reduced Graphene Oxide. *Nano Lett.* **2010**, *10*, 577–583.
26. Ding, Y. H.; Zhang, P.; Zhuo, Q.; Ren, H. M.; Yang, Z. M.; Jiang, Y. A Green Approach to the Synthesis of Reduced Graphene Oxide Nanosheets under UV Irradiation. *Nanotechnology* **2011**, 22.
27. Shul'ga, Y. M.; Vasilets, V. N.; Baskakov, S. A.; Muradyan, V. E.; Skryleva, E. A.; Parkhomenko, Y. N. Photoreduction of Graphite Oxide Nanosheets with Vacuum Ultraviolet Radiation. *High Energy Chem.* **2012**, *46*, 117–121.

28. Guardia, L.; Villar-Rodil, S.; Paredes, J. I.; Rozada, R.; Martinez-Alonso, A.; Tascon, J. M. D. UV Light Exposure of Aqueous Graphene Oxide Suspensions To Promote Their Direct Reduction, Formation of Graphene-Metal Nanoparticle Hybrids and Dye Degradation. *Carbon* **2012**, *50*, 1014–1024.
29. Kim, S. R.; Parvez, M. K.; Chhowalla, M. UV-Reduction of Graphene Oxide and Its Application as an Interfacial Layer To Reduce the Back-Transport Reactions in Dye-Sensitized Solar Cells. *Chem. Phys. Lett.* **2009**, *483*, 124–127.
30. Dreyer, D. R.; Park, S.; Bielawski, C. W.; Ruoff, R. S. The Chemistry of Graphene Oxide. *Chem. Soc. Rev.* **2010**, *39*, 228–240.
31. Lightcap, I. V.; Kamat, P. V. Fortification of CdSe Quantum Dots with Graphene Oxide. Excited State Interactions and Light Energy Conversion. *J. Am. Chem. Soc.* **2012**, *134*, 7109–7116.
32. Radich, J. G.; Dwyer, R.; Kamat, P. V. Cu_2S-Reduced Graphene Oxide Composite for High-Efficiency Quantum Dot Solar Cells. Overcoming the Redox Limitations of Polysulfide at the Counter Electrode. *J. Phys. Chem. Lett.* **2011**, *2*, 2453–2460.
33. Kamat, P. V. Graphene-Based Nanoassemblies for Energy Conversion. *J. Phys. Chem. Lett.* **2011**, *2*, 242–251.
34. Sun, S. R.; Gao, L. A.; Liu, Y. Q.; Sun, J. Assembly of CdSe Nanoparticles on Graphene for Low-Temperature Fabrication of Quantum Dot Sensitized Solar Cell. *Appl. Phys. Lett.* **2011**, 98.
35. Jia, L.; Wang, D. H.; Huang, Y. X.; Xu, A. W.; Yu, H. Q. Highly Durable N-Doped Graphene/CdS Nanocomposites with Enhanced Photocatalytic Hydrogen Evolution from Water under Visible Light Irradiation. *J. Phys. Chem. C* **2011**, *115*, 11466–11473.
36. Li, Q.; Guo, B. D.; Yu, J. G.; Ran, J. R.; Zhang, B. H.; Yan, H. J.; Gong, J. R. Highly Efficient Visible-Light-Driven Photocatalytic Hydrogen Production of CdS-Cluster-Decorated Graphene Nanosheets. *J. Am. Chem. Soc.* **2011**, *133*, 10878–10884.
37. Min, S. X.; Lu, G. X. Dye-Sensitized Reduced Graphene Oxide Photocatalysts for Highly Efficient Visible-Light-Driven Water Reduction. *J. Phys. Chem. C* **2011**, *115*, 13938–13945.
38. Park, H.; Howden, R. M.; Barr, M. C.; Bulovic, V.; Gleason, K.; Kong, J. Organic Solar Cells with Graphene Electrodes and Vapor Printed Poly(3,4-ethylenedioxythiophene) as the Hole Transporting Layers. *ACS Nano* **2012**, *6*, 6370–6377.
39. Chou, S. L.; Wang, J. Z.; Choucair, M.; Liu, H. K.; Stride, J. A.; Dou, S. X. Enhanced Reversible Lithium Storage in a Nanosize Silicon/Graphene Composite. *Electrochem. Commun.* **2010**, *12*, 303–306.
40. Wu, Z. S.; Ren, W. C.; Wen, L.; Gao, L. B.; Zhao, J. P.; Chen, Z. P.; Zhou, G. M.; Li, F.; Cheng, H. M. Graphene Anchored with Co_3O_4 Nanoparticles as Anode of Lithium Ion Batteries with Enhanced Reversible Capacity and Cyclic Performance. *ACS Nano* **2010**, *4*, 3187–3194.
41. Wang, B.; Park, J.; Wang, C. Y.; Ahn, H.; Wang, G. X. Mn_3O_4 Nanoparticles Embedded into Graphene Nanosheets: Preparation, Characterization, and Electrochemical Properties for Supercapacitors. *Electrochim. Acta* **2010**, *55*, 6812–6817.
42. Yan, J.; Wei, T.; Qiao, W. M.; Shao, B.; Zhao, Q. K.; Zhang, L. J.; Fan, Z. J. Rapid Microwave-Assisted Synthesis of Graphene Nanosheet/Co_3O_4 Composite for Supercapacitors. *Electrochim. Acta* **2010**, *55*, 6973–6978.
43. Wang, H. L.; Cui, L. F.; Yang, Y. A.; Casalongue, H. S.; Robinson, J. T.; Liang, Y. Y.; Cui, Y.; Dai, H. J. Mn_3O_4-Graphene Hybrid as a High-Capacity Anode Material for Lithium Ion Batteries. *J. Am. Chem. Soc.* **2010**, *132*, 13978–13980.
44. Yang, Y. Y.; Hu, Z. A.; Zhang, Z. Y.; Zhang, F. H.; Zhang, Y. J.; Liang, P. J.; Zhang, H. Y.; Wu, H. Y. Reduced Graphene Oxide-Nickel Oxide Composites with High Electrochemical Capacitive Performance. *Mater. Chem. Phys.* **2012**, *133*, 363–368.
45. Gao, H. C.; Xiao, F.; Ching, C. B.; Duan, H. W. High-Performance Asymmetric Supercapacitor Based on Graphene Hydrogel and Nanostructured MnO_2. *ACS Appl. Mater. Interfaces* **2012**, *4*, 2801–2810.
46. Zhao, Y. Q.; Zhao, D. D.; Tang, P. Y.; Wang, Y. M.; Xu, C. L.; Li, H. L. MnO_2/Graphene/Nickel Foam Composite as High Performance Supercapacitor Electrode *via* a Facile Electrochemical Deposition Strategy. *Mater. Lett.* **2012**, *76*, 127–130.
47. Yu, D. S.; Dai, L. M. Self-Assembled Graphene/Carbon Nanotube Hybrid Films for Supercapacitors. *J. Phys. Chem. Lett.* **2010**, *1*, 467–470.
48. Wang, H. L.; Hao, Q. L.; Yang, X. J.; Lu, L. D.; Wang, X. Effect of Graphene Oxide on the Properties of Its Composite with Polyaniline. *ACS Appl. Mater. Interfaces* **2010**, *2*, 821–828.
49. Xu, G. H.; Wang, N.; Wei, J. Y.; Lv, L. L.; Zhang, J. A.; Chen, Z. M.; Xu, Q. Preparation of Graphene Oxide/Polyaniline Nanocomposite with Assistance of Supercritical Carbon Dioxide for Supercapacitor Electrodes. *Ind. Eng. Chem. Res.* **2012**, *51*, 14390–14398.
50. Wu, X. Z.; Zhou, J.; Xing, W.; Wang, G. Q.; Cui, H. Y.; Zhuo, S. P.; Xue, Q. Z.; Yan, Z. F.; Qiao, S. Z. High-Rate Capacitive Performance of Graphene Aerogel with a Superhigh C/O Molar Ratio. *J. Mater. Chem.* **2012**, *22*, 23186–23193.
51. Radich, J. G.; Kamat, P. V. Origin of Reduced Graphene Oxide Enhancements in Electrochemical Energy Storage. *ACS Catal.* **2012**, *2*, 807–816.
52. Bhardwaj, T.; Antic, A.; Pavan, B.; Barone, V.; Fahlman, B. D. Enhanced Electrochemical Lithium Storage by Graphene Nanoribbons. *J. Am. Chem. Soc.* **2010**, *132*, 12556–12558.
53. Pollak, E.; Geng, B. S.; Jeon, K. J.; Lucas, I. T.; Richardson, T. J.; Wang, F.; Kostecki, R. The Interaction of Li^+ with Single-Layer and Few-Layer Graphene. *Nano Lett.* **2010**, *10*, 3386–3388.
54. Uthaisar, C.; Barone, V. Edge Effects on the Characteristics of Li^+ Diffusion in Graphene. *Nano Lett.* **2010**, *10*, 2838–2842.
55. Stoller, M. D.; Murali, S.; Quarles, N.; Zhu, Y. W.; Potts, J. R.; Zhu, X. J.; Ha, H. W.; Ruoff, R. S. Activated Graphene as a Cathode Material for Li-Ion Hybrid Supercapacitors. *Phys. Chem. Chem. Phys.* **2012**, *14*, 3388–3391.
56. Zhang, L. L.; Zhao, X.; Stoller, M. D.; Zhu, Y. W.; Ji, H. X.; Murali, S.; Wu, Y. P.; Perales, S.; Clevenger, B.; Ruoff, R. S. Highly Conductive and Porous Activated Reduced Graphene Oxide Films for High-Power Supercapacitors. *Nano Lett.* **2012**, *12*, 1806–1812.
57. Choi, B. G.; Yang, M.; Hong, W. H.; Choi, J. W.; Huh, Y. S. 3D Macroporous Graphene Frameworks for Supercapacitors with High Energy and Power Densities. *ACS Nano* **2012**, *6*, 4020–4028.
58. Xu, Z. W.; Li, Z.; Holt, C. M. B.; Tan, X. H.; Wang, H. L.; Amirkhiz, B. S.; Stephenson, T.; Mitlin, D. Electrochemical Supercapacitor Electrodes from Sponge-like Graphene Nanoarchitectures with Ultrahigh Power Density. *J. Phys. Chem. Lett.* **2012**, *3*, 2928–2933.
59. Zhu, Y. W.; Murali, S.; Stoller, M. D.; Ganesh, K. J.; Cai, W. W.; Ferreira, P. J.; Pirkle, A.; Wallace, R. M.; Cychosz, K. A.; Thommes, M.; *et al.* Carbon-Based Supercapacitors Produced by Activation of Graphene. *Science* **2011**, *332*, 1537–1541.
60. Shang, C.; Liu, Z. P. Origin and Activity of Gold Nanoparticles as Aerobic Oxidation Catalysts in Aqueous Solution. *J. Am. Chem. Soc.* **2011**, *133*, 9938–9947.
61. Zan, R.; Bangert, U.; Ramasse, Q.; Novoselov, K. S. Interaction of Metals with Suspended Graphene Observed by Transmission Electron Microscopy. *J. Phys. Chem. Lett.* **2012**, *3*, 953–958.
62. Anpo, M.; Shima, T.; Kubokawa, Y. Electron-Sping-Resonance and Photoluminescence Evidence for the Photocatalytic Formation of Hydroxyl Radicals on Small TiO_2 Particles. *Chem. Lett.* **1985**, 1799–1802.
63. Cunningham, J.; Srijaranai, S. Isotope-Effect Evidence for Hydroxyl Radical Involvement in Alcohol Photo-oxidation Sensitized by TiO_2 in Aqueous Suspension. *J. Photochem. Photobiol., A:* **1988**, *43*, 329–335.
64. Lawless, D.; Serpone, N.; Meisel, D. Role of $OH^•$ Radicals and Trapped Holes in Photocatalysis—A Pulse-Radiolysis Study. *J. Phys. Chem.* **1991**, *95*, 5166–5170.
65. Dreizler, A. M.; Roduner, E. Reaction Kinetics of Hydroxyl Radicals with Model Compounds of Fuel Cell Polymer Membranes. *Fuel Cells* **2012**, *12*, 132–140.

66. Noel, J.-M.; Latus, A.; Lagrost, C.; Volanschi, E.; Hapiot, P. Evidence for OH Radical Production during Electrocatalysis of Oxygen Reduction on Pt Surfaces: Consequences and Application. *J. Am. Chem. Soc.* **2012**, *134*, 2835–2841.
67. Bryantsev, V. S.; Giordani, V.; Walker, W.; Blanco, M.; Zecevic, S.; Sasaki, K.; Uddin, J.; Addison, D.; Chase, G. V. Predicting Solvent Stability in Aprotic Electrolyte Li-Air Batteries: Nucleophilic Substitution by the Superoxide Anion Radical ($O_2^{-\bullet}$). *J. Phys. Chem. A* **2011**, *115*, 12399–12409.
68. Freunberger, S. A.; Chen, Y.; Peng, Z.; Griffin, J. M.; Hardwick, L. J.; Barde, F.; Novak, P.; Bruce, P. G. Reactions in the Rechargeable Lithium-O_2 Battery with Alkyl Carbonate Electrolytes. *J. Am. Chem. Soc.* **2011**, *133*, 8040–8047.
69. McCloskey, B. D.; Bethune, D. S.; Shelby, R. M.; Girishkumar, G.; Luntz, A. C. Solvents' Critical Role in Nonaqueous Lithium-Oxygen Battery Electrochemistry. *J. Phys. Chem. Lett.* **2011**, *2*, 1161–1166.
70. Muszynski, R.; Seger, B.; Kamat, P. Decorating Graphene Sheets with Gold Nanoparticles. *J. Phys. Chem. C* **2008**, *112*, 5263–5266.
71. Ishibashi, K.; Fujishima, A.; Watanabe, T.; Hashimoto, K. Detection of Active Oxidative Species in TiO_2 Photocatalysis Using the Fluorescence Technique. *Electrochem. Commun.* **2000**, *2*, 207–210.
72. Ishibashi, K.; Fujishima, A.; Watanabe, T.; Hashimoto, K. Quantum Yields of Active Oxidative Species Formed on TiO_2 Photocatalyst. *J. Photochem. Photobiol., A* **2000**, *134*, 139–142.
73. Hirakawa, T.; Nosaka, Y. Properties of $O_2^{-\bullet}$ and $OH^{\bullet}$ Formed in TiO_2 Aqueous Suspensions by Photocatalytic Reaction and the Influence of H_2O_2 and Some Ions. *Langmuir* **2002**, *18*, 3247–3254.
74. Milosavljevic, B. H.; LaVerne, J. A. Pulse Radiolysis of Aqueous Thiocyanate Solution. *J. Phys. Chem. A* **2005**, *109*, 165–168.
75. Chin, M.; Wine, P. H. A Temperature-Dependent Kinetics Study of the Aqueous Phase Reactions $OH + SCN^- \rightarrow SCNOH^-$ and $SCN + SCN^- \rightarrow (SCN)_2^-$. *J. Photochem. Photobiol., A* **1992**, *69*, 17–25.
76. Carlson, M. T.; Green, A. J.; Richardson, H. H. Superheating Water by CW Excitation of Gold Nanodots. *Nano Lett.* **2012**, *12*, 1534–1537.
77. Anbar, M.; Meyerstein, D.; Neta, P. The Reactivity of Aromatic Compounds toward Hydroxyl Radicals. *J. Phys. Chem.* **1966**, *70*, 2660–2662.
78. Peller, J.; Wiest, O.; Kamat, P. V. Hydroxyl Radical's Role in the Remediation of a Common Herbicide, 2,4-Dichlorophenoxyacetic Acid (2,4-D). *J. Phys. Chem. A* **2004**, *108*, 10925–10933.
79. Kumar, P. V.; Bernardi, M.; Grossman, J. C. The Impact of Functionalization on the Stability, Work Function, and Photoluminescence of Reduced Graphene Oxide. *ACS Nano* **2013**, *7*, 1638–1645.
80. Zhu, C. Z.; Dong, S. J. Recent Progress in Graphene-Based Nanomaterials as Advanced Electrocatalysts towards Oxygen Reduction Reaction. *Nanoscale* **2013**, *5*, 1753–1767.
81. Fu, X. G.; Liu, Y. R.; Cao, X. P.; Jin, J. T.; Liu, Q.; Zhang, J. Y. FeCo-N-x Embedded Graphene as High Performance Catalysts for Oxygen Reduction Reaction. *Appl. Catal., B* **2013**, *130*, 143–151.
82. Cho, S. H.; Yang, H. N.; Lee, D. C.; Park, S. H.; Kim, W. J. Electrochemical Properties of Pt/Graphene Intercalated by Carbon Black and Its Application in Polymer Electrolyte Membrane Fuel Cell. *J. Power Sources* **2013**, *225*, 200–206.
83. Tripachev, O.; Bogdanovskaya, V.; Tarasevich, M.; Andoralov, V. Gold Autodeactivation during Oxygen Electroreduction Studied by Electrochemical Impedance Spectroscopy. *J. Electroanal. Chem.* **2012**, *683*, 21–24.
84. Noel, J. M.; Yu, Y.; Mirkin, M. V. Dissolution of Pt at Moderately Negative Potentials during Oxygen Reduction in Water and Organic Media. *Langmuir* **2013**, *29*, 1346–1350.